-RESEARCH PAPER-

International Journal of Mining and Geo-Engineering

IJMGE

IJMGE 57-2 (2023) 183-194

DOI: 10.22059/IJMGE.2023.352048.595007

Reconstruction of geological images based on an adaptive spatial domain filter: an example to introduce quantum computation to geosciences

Sadegh Kalantari [a], Ali Madadi [a], Mehdi Ramezani [b, *]

[a] *Department of Electrical Engineering, Tafresh University, Tafresh, Iran.*

[b] *Department of Mathematics, Tafresh University, Tafresh, Iran.*

Article History:

Received: 04 December 2022.

Revised: 15 January 2023.

Accepted: 08 February 2023.

ABSTRACT

Reconstruction of geological images using partial measurement is one of the most important topics in geosciences. In many methods, this is done using training images and very complex models, which increase the computational complexity. In the first part of the article, a simple method based on spatial domain filters, such as median and mean filters is presented in order to reconstruct geological images. One of the most significant characteristics of this method is that it does not need the training image; moreover, its computational complexity is less than the other advanced methods. Via this method, it is easy to reconstruct binary, continuous, and three-dimensional images. The results show that the reconstruction accuracy of the proposed method is also acceptable. In the second part of the article, in order to introduce quantum computing to geosciences and encourage researchers to work on this issue, a quantum median filter is proposed to reconstruct geological images. According to the results, this method has much less computational complexity than classical methods, such as DS. Also, its results are acceptable in terms of reconstruction rate. Due to the high speed of quantum algorithms and the widespread use of quantum computers in the near future, it is necessary for researchers in this field to become more familiar with quantum computing.

Keywords: *: Image reconstruction, Geosciences, Spatial filter, Computational complexity, Quantum computing, Quantum image processing.*

1. Introduction

Estimating different physical parameters in underground aquifers using a small number of samples is one of the most important issues in geosciences. In order to study and examine the aquifers' behavior in a field, they are sampled by geologists. However, sampling all parts of a field is not possible due to practical and financial constraints [1]. That is why sampling is done randomly in some parts of a field; therefore, reconstructing a field using few samples can be considered as an image reconstruction problem. The parts whose pixel values are unknown (or NAN) must be filled using some techniques. The stronger these techniques, the fewer samples would be needed to reconstruct the image field. For this purpose, the statistical knowledge of geologists is usually used in the reconstruction process. This knowledge is often presented in the form of a model whose shape might be a histogram, variogram, or a training image. These are called geostatistical models.

One of the geostatistical models used in this field is the multi-Gaussian distribution. Since Gaussian distributions include useful mathematical features, they are used in modelling spatial variables [2,3]. Due to inherent limitations of such distributions in terms of their variability, the output images are often smooth and incompatible with realistic heterogeneities in geological images. Also, the output images do not have appropriate connectivity [4].

The other models used in this area of science are called kriging methods. These methods are based on interpolation [5,6]. Kriging is an estimation method based on a weighted moving average. Smoothing the high frequency parts of the image during interpolation is one of the features of the kriging model. This means that the variance of the estimated samples looks very close to the real points, and there are fewer differences compared to the real points. One of the advantages of this method is its low computational complexity.

There are also some other sets of methods which are based on training images [7-11]. Among these methods are multiple-point simulation methods. Using training images, geologists can express geological concepts; therefore, the statistical model used in these methods is similar to the one used in the training image. For simulation, a grid is first created. At the beginning of the simulation, only the values of the sampled points are known, and the rest of the network has a NAN value. The simulation grid is swept in a random direction. In each simulation node, the window around the node is considered as a among data event. Then, of the existing patterns in the training image, the pattern which satisfies the hard data is selected, and its value is used for filling the data event.

Multiple-point simulation methods are divided into patch-based and pixel-based methods. In pixel-based methods, when the equivalent of a data event is found in the training image, only its central pixel is replaced in the simulation grid. On the other hand, in patch-based methods, a substantial part of the found pattern is transferred to the simulation grid. The DS algorithm is one of the widely used pixel-based methods [8]. In this method, instead of forming a database from the training image, the focus is on finding the most similar pattern in the training image. For each data event, its distance from the patterns of the training image is calculated, and the pattern with the smallest distance is selected, and its central pixel is placed in the data event. One of the advantages of this algorithm is the ability to simulate binary and continuous images and solve the problem of dealing with non-stationary images. However, it is

* Corresponding author: *E-mail address:* ramezani@tafreshu.ac.ir (M. Ramezani).

too slow due to the difficulty of filling the simulation grid pixel by pixel and searching for similar pixels in the training image. In pixel-based methods, the simulation grids are filled pixel by pixel. Also, in these methods, doing a search to find the matching pixels in the training image is inevitable; therefore, their processing speed is rather low.

Finding a pattern similar to a data event is called template matching. During the execution of the simulation algorithm, researchers have to deal with a great number of template matching problems. This itself increases the computational complexity. In order to solve the problem of template-matching, some image patterns are usually extracted from the training image and put into the database. In these methods, fixed sized patterns are extracted from the training image during the preprocessing phase. If the size of such patterns is small, the large-scale behavior of the image will not be modelled well, and if the size of the patterns is big, the computational complexity will also be high. To overcome this problem, a multi-scale structure is usually used which in turn increases the computational complexity again [12].

The majority of multiple-point simulation methods are sequential. In these methods, the simulation grid is filled sequentially, and the pattern which is put in the simulation grid is highly dependent on the selected pattern in the previous stage. Therefore, if the template matching does not lead to selecting an appropriate pattern, this negatively affects the patterns selected in the next stages. This results in error accumulation and reduces the quality of the simulated image [13]. Some methods which have been proposed recently are not sequential. They are called optimization-based methods [2,9,13]. These methods consider the image simulation problem as an optimization one. In the Yang method, a global optimization-based algorithm has been proposed which defines a cost function that expresses the difference between the output realization and the training image [13]. To achieve the simulated image, this cost function is minimized using an iterative multi-scale method in each iteration. The positive point about this method is the creation of various patterns in the simulated image. On the downside, tuning algorithm parameters, such as the number of appropriate iterations at each scale in order to achieve an acceptable solution is difficult.

In [9], another model which is called the sparse representation has been used to solve the optimization problem. In this model, it is assumed that an image patch can be reconstructed with a linear combination of a limited number of dictionary atoms. Since only a few atoms of dictionary are combined together in order to create an image patch, this method is able to create a wide variety of patterns that are not similar to training image patterns. However, one of the disadvantages of this method is the blurring caused by the averaging the simulated patches, which negatively affects the output image. Another problem is the high computational complexity, which is due to solving an optimization problem.

In [2], another model to solve the problem of image reconstruction has been used. This model which does not need a training image is called ULEM. In this method, an analytical edge model is employed. ULEM is based on the assumption that within a suitable window size, binary images can be described using a linear edge model. However, since this method is based on solving an optimization problem in a great number of iterations, its computational complexity is very high. In all training image-based methods, choosing an appropriate training image is a fundamental challenge. If the wrong training image is selected, the simulated image will not be reliable [2]. Template matching is usually used to select the appropriate training image. It is a widely-used method for matching different templates; however, its computational complexity is very high. In practice, the reconstructed images are three-dimensional and very large. This can cause a significant increase in the computational complexity. Thus, one approach is to use the methods that have lower computational complexity and yield acceptable results.

Recently, advances have been made in the field of quantum computing and quantum image processing. In reference [14], which is a review article, some applications of quantum computing, such as reconstruction of porous media, simulating fluid flow, and big data analysis in geosciences have been discussed. Quantum technology reduces the computational complexity of algorithms. Quantum algorithms are able to solve many mathematical problems in a shorter time. Making significant progress in geosciences, especially in reconstruction and simulation, are dependent on advancements in computer hardware and software technology. These days, it is essential for geologists to become more familiar with quantum algorithms in order to take advantage of them when they are available.

One of the important features of quantum computing is its ability to solve least squares problem at a much faster speed. In general, image reconstruction can be considered as a static system identification problem. According to the samples in the image, estimating the missing pixels leads to solving a linear problem. One of the simplest and most widely used methods of data estimation and model fitting is the least squares method. The mentioned problem is represented as the linear equation in which $Ax = b$. To solve this problem, n-bit sequences must be stored. The computational complexity of storing n-bit sequences is $O(n2^n)$ in classical computers, but the order of $O(n)$ in quantum computers. When performing operations on sequences, such as bitwise inversion, classical computers need $O(2^n)$, while quantum computers only need $O(1)$ [15]. The best available classical method to solve this problem is the conjugate gradient method, which requires $O(ksn)$. To solve sparse matrices, k is the condition number, which is the ratio of the largest eigenvalue to the smallest one, and s is the sparsity value or the number of non-zero values in each row. On the other hand, there is the method called the HHL quantum algorithm, which solves the least squares problem with $O(kslog_2n)$ [16]. The HHL quantum algorithm greatly reduces the computational cost in high-dimensional problems, such as three-dimensional images.

In the second part of the article, an image reconstruction method based on the classical median filter will be presented. It has yielded acceptable results in terms of speed and reconstruction accuracy compared to other methods. In the proposed method, no training image is needed, and reconstruction can be done with relatively good speed and accuracy, even with small samples. In order to introduce quantum computing to geosciences, section 3 explains some preliminaries of quantum computing. In section 4, a quantum median filter will be presented to reconstruct geological images, and quantum and classical computations will be compared. In section 5, a summary of the research is presented.

2. The proposed reconstruction method based on the classical median filter

In image reconstruction, the value of some points is known, and the value of the other points must be determined using the available samples. Noise removal is one of the methods by which images are reconstructed. The aim of this study is to use this method in geological image reconstruction. The Median filter is a commonly used method in image processing to remove salt and pepper noise. This filter falls under the category of spatial domain filters. In the original version of this method, a fixed window is assumed to exist around each pixel of the noisy image. Then, the median value of the pixels is placed in the center of the window. The important thing about salt and pepper noise is that the pixels destroyed by this noise appear as the maximum and minimum gray levels in the image. To improve the performance of this filter, different ideas have been proposed [17-19]. One is to apply the window size adaptively. That is, the size of the window around each noisy pixel is determined according to the conditions and values of the neighboring pixels. In this article, in order to use these kinds of filters to reconstruct the image, it is assumed that the parts whose value is unknown in the sampled image are the noise points. Therefore, an adaptive window is considered around the non-valued pixels, and the desired pixel value is estimated using the samples within that window. To choose the right window size, the idea proposed in reference [18] was employed. It should be noted that in [18], this idea is used to determine the noisy point; but in this paper that idea is used to determine the appropriate window size in order to estimate those non-valued pixels. The steps taken during this algorithm are as follow: first, a 3×3 window around unknown pixels is considered. Then, the window size is increased by one

unit around that pixel continues up to the point where the minimum and maximum values of two consecutive windows are equal to each other. To avoid errors and the use of irrelevant data, the window continues to be enlarged to a maximum size of 43. This threshold was selected after testing the proposed algorithm on different images. Take figure 1 as an example. In this picture, the average reconstruction rate is shown according to the window size in sampling percentages of 3% and 5% for the Wall-stone and Delta images. As shown, increasing the window size more than 43 leads to a significant decrease in reconstruction accuracy. Using a threshold of 43, we can use the information of the neighboring pixels in this application. In addition, in this way, the other irrelevant objects in the image do not interfere with pixel estimation. It should be noted that for an original image I_o and a reconstructed image I_r, the percentage of image reconstruction rate is obtained through equation (1). In this equation, N is the total number of image pixels, and (x, y) is the corresponding position in the image.

$$A = (1 - \frac{1}{N}\sum_{(x_1,x_2)\in P}|I_o(x,y) - I_r(x,y)| \times 100) \quad (1)$$

After determining the appropriate window size, all the samples within this window are extracted. Then, their median and mean values are calculated. Eventually, the average of the mean and median is considered as the pixel value. The reason for using the average of the median and the mean is that neither of them (neither the median nor the mean) can be a good representative of several numbers on their own. To make it clear, suppose that the central pixel is noisy, and the window around it has the values of non-noisy pixels as {1, 10, 62, 66, 67, 189, 241, 234, 203}.

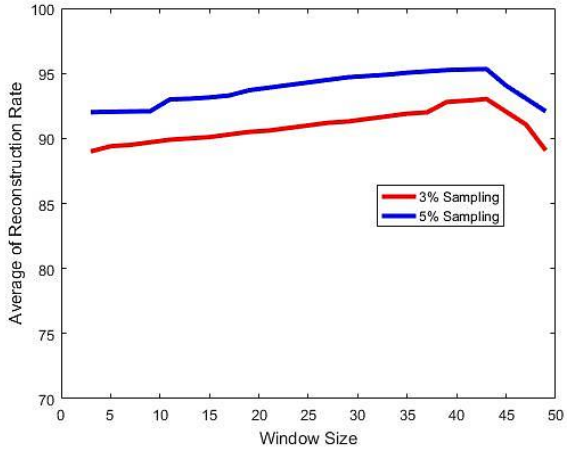

Figure1. The average reconstruction rate for the wall-stone and Delta image for sampling percentage 3% and 5%.

The central pixel within this window should be replaced with a non-noise value. The mean value of these pixels is equal to 119, and their median value is equal to 67. In this example, the difference between these two numbers is about 52. If we only use the median or average values, we cannot obtain an acceptable result. The reason is that, according to the condition of the image in this window, we cannot determine whether the mean is a good representative or the median is a better representative. Therefore, to minimize the error, it seems more logical to choose the average of median and mean for the central pixel. In other words, the information of both the median and mean are used in this case. The other combinations related to the mean and median including their weighted averages may lead to better results. However, to avoid increasing the computational complexity, the simplest solution (the average of two parameters) was chosen. That is because the average is an easy choice for two statistical parameters. The reconstruction algorithm of this paper is listedwithinin more detail in Table 1. Some of the parameters used in the algorithm are as follows.

w: window size

w_{max}: The largest acceptable window size

$a_{i,j}^{min}(w)$: The smallest intensity in the window with the centrality of (i, j).

$a_{i,j}^{max}(w)$: The largest intensity within the window with the centrality of (i, j).

$a_{i,j}^{mean}(w)$: The average of pixels within the window with the size of w to the centrality of (i, j). Needless to say, the value of the gray level in those pixels must not be equal to either minimum or maximum value of gray level within the window.

$a_{i,j}^{med}(w)$: The median of pixels within the window with the size of w to the centrality of (i, j). Needless to say, the value of the gray level in those pixels must not be equal to either minimum or maximum value of the gray level within the window.

This method allows the users to reconstruct binary, continuous, and three-dimensional images. It should be noted that in binary images, the estimated pixel may have a continuous value. To convert it into a binary image, the thresholding method in the article [9] was used. This method was developed by the authors of this article. In this thresholding method, the histogram is filtered with a 50-point hamming window, and the deepest valley between the two peaks is considered as the threshold value. To reconstruct 3D images, all we needed to do was to extract 3D cubic patches from the image. After calculating a sufficient number of samples, we used them to estimate the desired pixel. In this article, due to a lack of access to real data, geological training images available in [20, 21] were used. These images have important features in terms of data dispersion. For this reason, they were used to test simulation and reconstruction algorithms. It is highly likely that the methods which yield good results on these images will have acceptable performance on real data [20]. In order to check the efficiency of the proposed method and compare it with other methods, tests were performed on 2D and 3D training images of figure 2. The results are shown in figures 3 to 7. For comparison, DS and ULEM methods were used [2, 8]. ULEM is similar to the proposed method in that none of them has a training image. Needless to mention, DS is one of the conventional reconstruction methods in this field that uses a training image.

It should be noted that the codes of the continuous version of the ULEM method were obtained from its authors. As for the DS method, the code published by the authors was used [21]. DS algorithm parameters were set as $r = 20$, $n_{DS} = 50$ and $r_{DS} = 1$, and in the ULEM method $N_{iters} = 1$, $\lambda = 1$, and $\eta = 15$. As shown in figures 3 and 4, the proposed method has better results compared to the other two methods, both visually and in terms of the reconstruction rate criterion. Also, according to figures 6 and 7, the proposed method has performed better in all sampling rates. In the proposed method, the average value of the median and the mean of the samples in the window is used to estimate a pixel. This process must be done for all pixels of the image. The computational complexity of the average is $O(n)$. Using the cube sort method, we reached the same computational complexity in the proposed algorithm. Therefore, assuming a m size patch for a $2^n \times 2^n$ image, the computational complexity of the proposed method will be the order of $O(m2^{2n})$. In the ULEM method, due to the use of the gradient descent algorithm, the computational complexity is the order of $O(k2^{2n}m^2)$, where k is the number of iterations and m is the patch size [2]. In gradient descent, a big number is usually chosen for k in order to reach the optimal solution. Since the extracted patches have maximum overlap and considering the size of the window used in the ULEM method, the number of patches extracted from the image is relatively close to the total number of pixels. As an example, in an image with a size of 200×200, which has a total of 40,000 pixels, there are 39,204 patches with size of 3×3. In the DS method, template matching is used. In template matching, m size patch is convolved with the whole image. Therefore, the computational complexity of the DS method is at least $O(2^{4n}m^2)$ [8]. The analysis shows that the computational complexity of the proposed method is much lower than the other methods. In order to practically compare the speed of the algorithms, tests have been performed on the Wall-Stone image, and the execution time for the algorithms is shown in figure 8. In this figure, t(A/B) shows the ratio of the execution time of algorithm A to algorithm B. Larger

Table 1. The proposed classical algorithm for the reconstruction of geological images.

Convert all NAN points of the incomplete image to salt and pepper noise (replace with values of 0 or 255).
Do steps 1 to 5 for all noisy points with position (i, j) :

1- Initialize $w = 3$ and $w_{max} = 43$.
2- Calculate the values $a_{i,j}^{min}(w)$, $a_{i,j}^{max}(w)$, $a_{i,j}^{min}(w+2)$ and $a_{i,j}^{max}(w+2)$.
3- Increase the size of the window $(w = w + 2)$ until $a_{i,j}^{min}(w) \neq a_{i,j}^{min}(w+2)$, $a_{i,j}^{max}(w) \neq a_{i,j}^{max}(w+2)$ and $w < w_{max}$.
4- Calculate $a_{i,j}^{min}(w)$ and $a_{i,j}^{med}(w)$.
5- Place $f_{i,j} = (a_{i,j}^{med}(w) + a_{i,j}^{mean}(w))/2$.
6- If the image is binary, convert the output image into a binary image using the thresholding method in the reference [9].

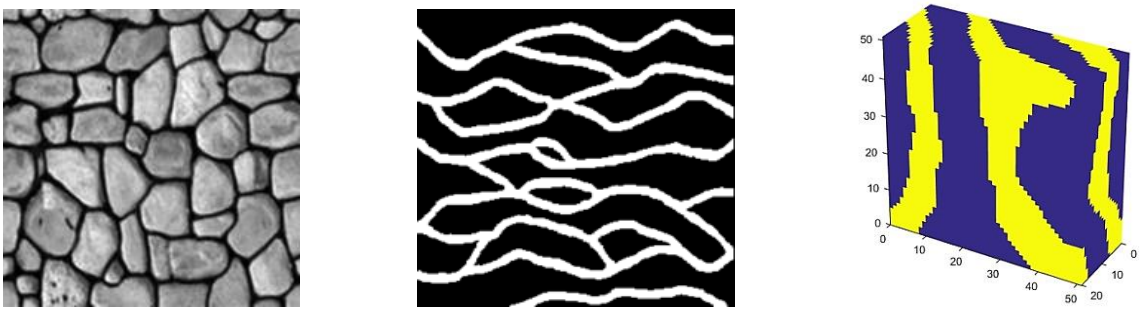

(a) (b) (c)

Figure 2. The training images used in this paper: (a) Wall-Stone, (b) Ti-Channel, (c) Delta.

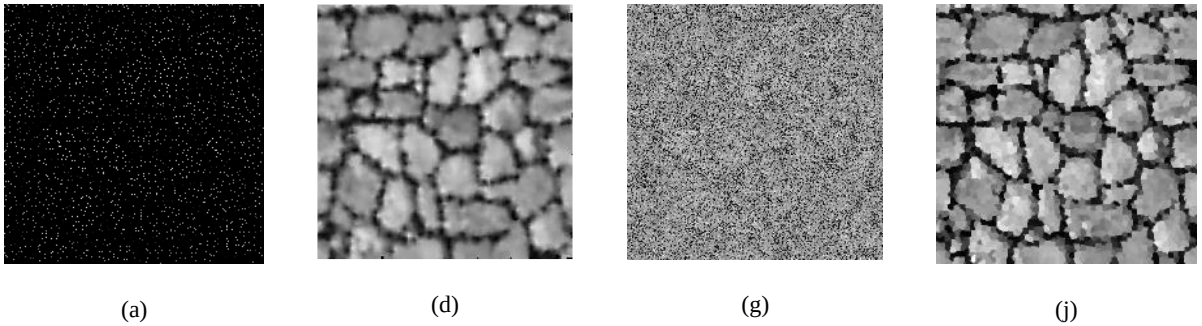

(a) (d) (g) (j)

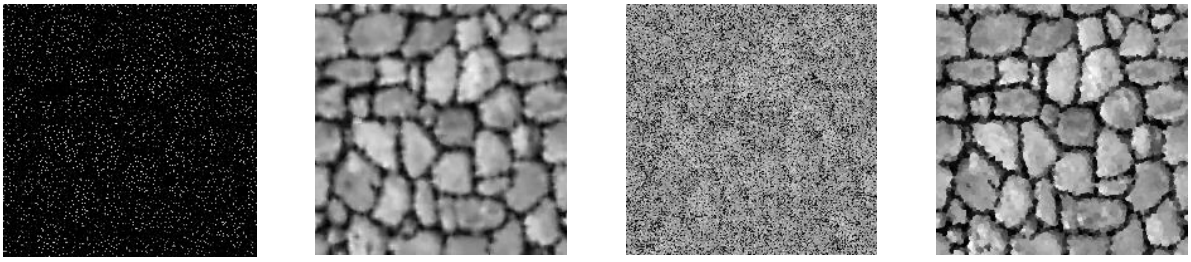

(b) (e) (h) (k)

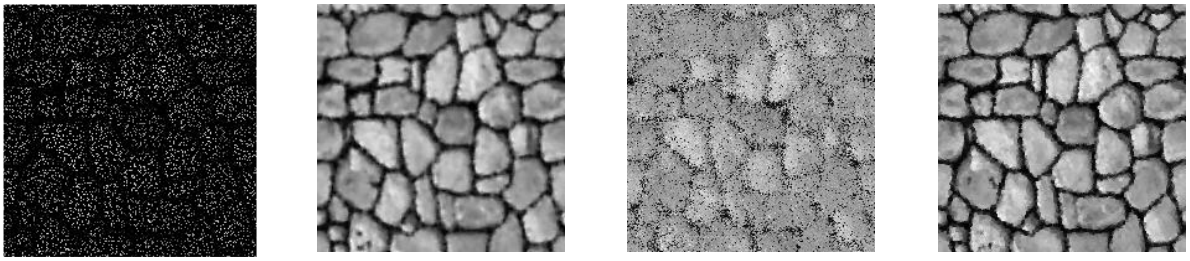

(c) (f) (i) (l)

Figure 3. The reconstruction results of ULEM, DS, and the proposed method for the wall-stone Image: (a) 5% sampling Image, (b) 8% sampling image, (c) 16% sampling image, (d-f) results for ULEM, (g-i) results for DS, (j-l) results for proposed method.

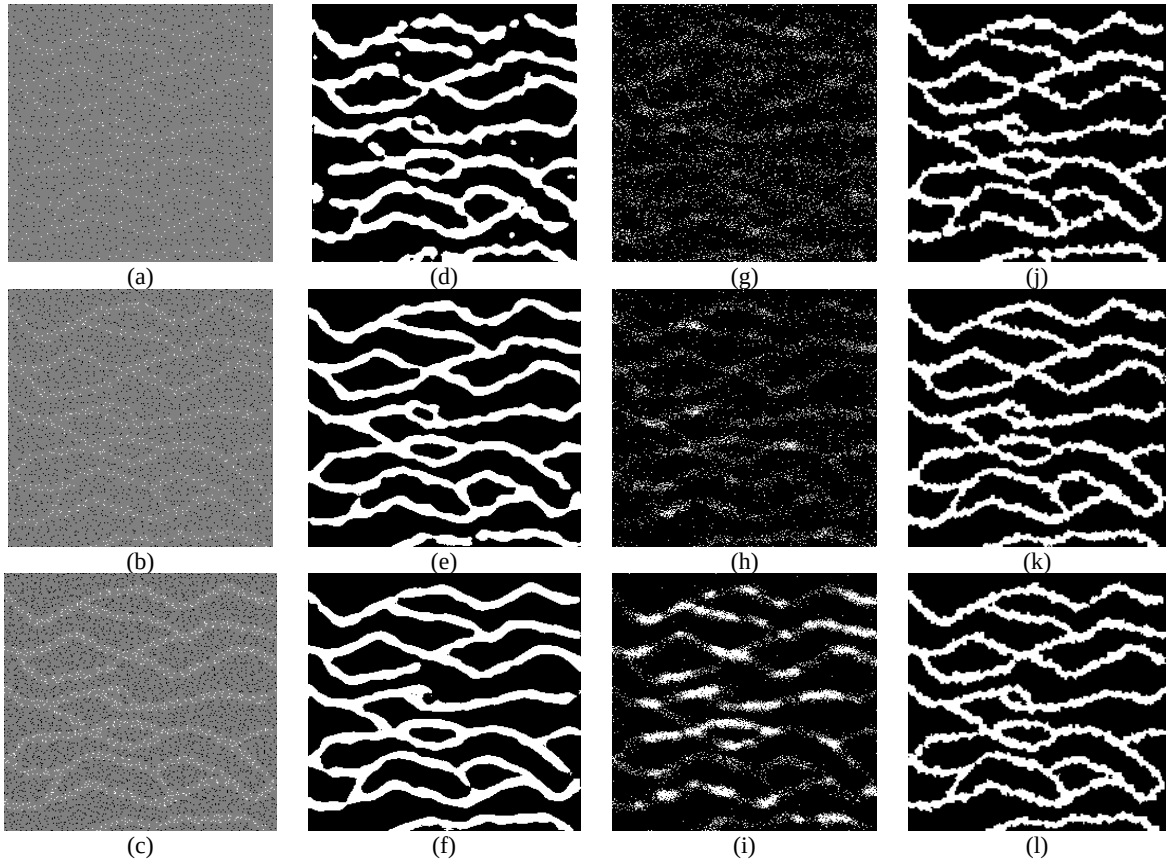

Figure 4. The reconstruction results of the ULEM, DS and the proposed method for Ti-channel image: (a) 3% sampling Image, (b) 5% sampling Image, (c) 8% sampling Image, (d-f) results for ULEM, (g-i) results for DS,(j-l) results for proposed method.

number indicates that algorithm A is slower than algorithm B. All the tests were performed on a computer with a Corei7, 6GB RAM, and on MATLAB 2016. According to figure 8, ULEM is faster than DS, and the proposed method is much faster compared to ULEM. Also, the results indicate that the reconstruction accuracy of the proposed method is acceptable in terms of both quantity and quality compared to the other methods. It should be noted that the proposed method has achieved the above results without need to use the training image.

3. An overview of quantum computing

Richard Feynman first proposed that quantum systems could be simulated using a special version of computation based on quantum mechanics. On the other hand, simulating systems with more than a few particles are very complicated in classical computation [22]. According to Moore's law, the efficiency of computers doubles every 2-3 years [23]. Since a limited number of transistors can be used inside the electronic chips, and complexities involved in producing such electronic devices with a large number of transistors, this law was on the verge of being violated. With the advent of quantum technology, this became closer to reality. Due to the use of quantum properties, such as superposition and entanglement, this technology solves the relevant problems at much faster speed. In 1994, Shore presented a quantum algorithm for solving the integer factorization problem with polynomial time [23]. Also, for conducting a search in an irregular set with quadratic speedup, Graver's algorithm was presented [23]. These two algorithms were good indicators to prove the extraordinary power of quantum computing compared to classical ones due to the significant reduction of the computational complexity. In recent years, studies have been conducted in various fields, including control, finance, chemistry, mathematics, biology, code breaking, sand image processing on the applications of quantum computing. However, so far, very few studies have been carried out on the application of quantum computing in geosciences. For this reason, in this article, after a brief introduction of quantum computing, a version of the quantum median filter will be presented for image reconstruction, and its computational complexity will be compared to classical methods.

A quantum computer is a machine that uses the principles of quantum mechanics to solve various problems [22]. Quantum computers process quantum bits or qubits as units of information. Unlike classical bits which only have a value of 0 or 1, quantum bits can have both states at the same time. This is one of the principles of quantum computing, which is known as superposition of states.

The numbers 0 and 1 can represent the downward and upward spin of atoms. In quantum computation, 0 and 1 are not regular numbers. They are two-dimensional vectors, which in Dirac's notation are in the form $|0\rangle = (1\ \ 0)^T$ and $|1\rangle = (0\ \ 1)^T$ respectively, where T means the conjugate transpose. A general qubit in terms of unit vector in a 2D Hilbert space is a superposition of these two states, shown as:

$$|\psi\rangle = \alpha|0\rangle + \beta|1\rangle = \alpha\binom{1}{0} + \beta\binom{0}{1} \quad (2)$$

Complex numbers α and β are called probability amplitudes, which indicate the probability of finding a qubit in the state $|0\rangle$ or $|1\rangle$. The next difference is that when measuring a qubit, the results is 0 or 1 with a probability of $|\alpha|^2$ or $|\beta|^2$ respectively. Since $|\alpha|^2 + |\beta|^2 = 1$, so:

$$|\psi\rangle = cos\frac{\theta}{2}|0\rangle + exp^{i\varphi}sin\frac{\theta}{2}|1\rangle \quad (3)$$

θ and φ are real numbers defined on a single three-dimensional space called the Bloch sphere. This space is shown in figure 9. The key point in quantum computers is that even though all computations can be done simultaneously on all states, they will collapse to one state if a measurement is done. As a result, at the moment of measurement, only

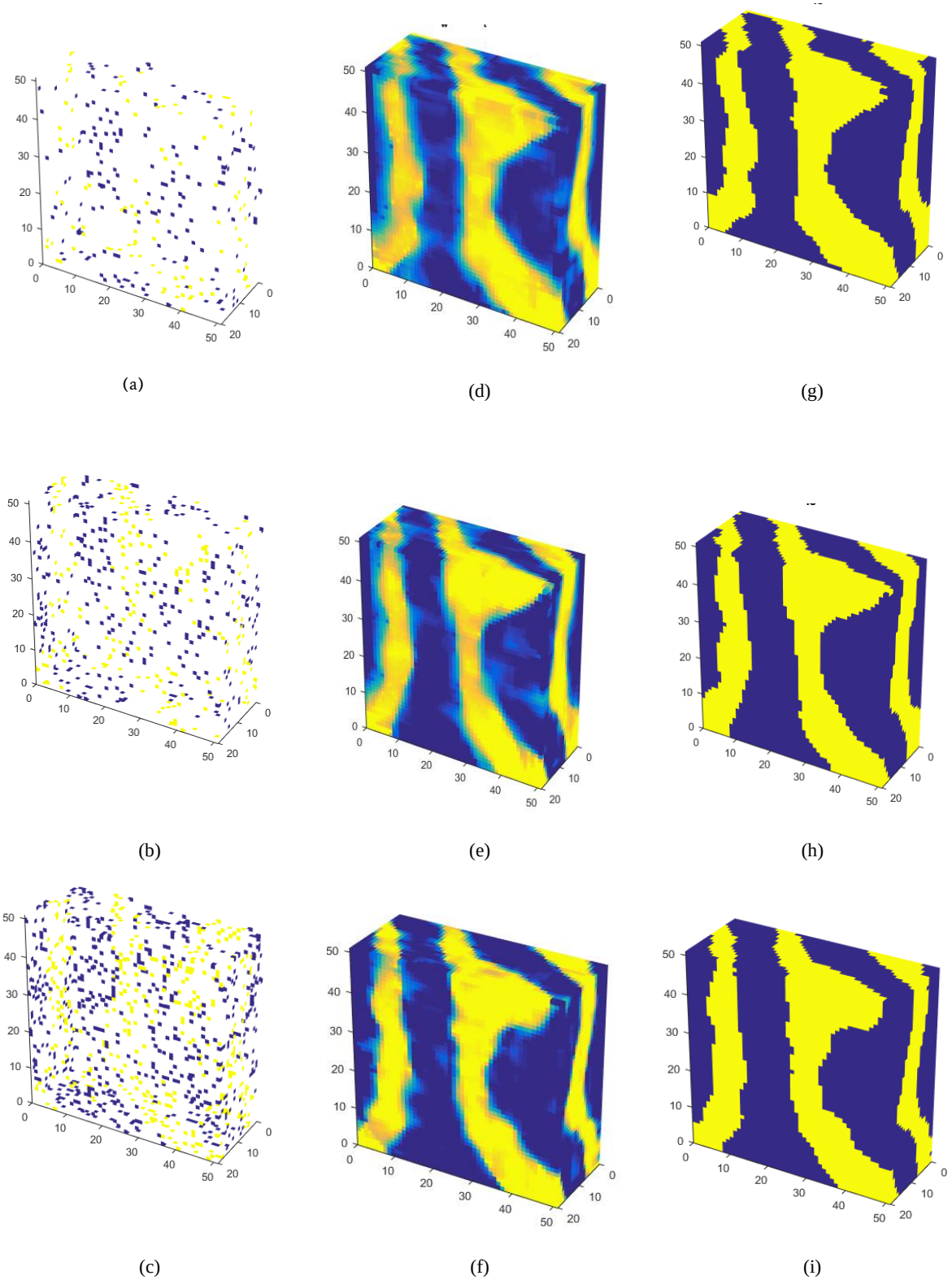

Figure 5. The results of proposed method for delta binary image: (a) 3% sampling, (b) 5% sampling, (c) 10% sampling, (d-f) output image before thresholding, (g) final image with Reconstruction Rate=93.09%, (h) final image with Reconstruction Rate=95.33%, (i) final image with Reconstruction Rate=96.96%.

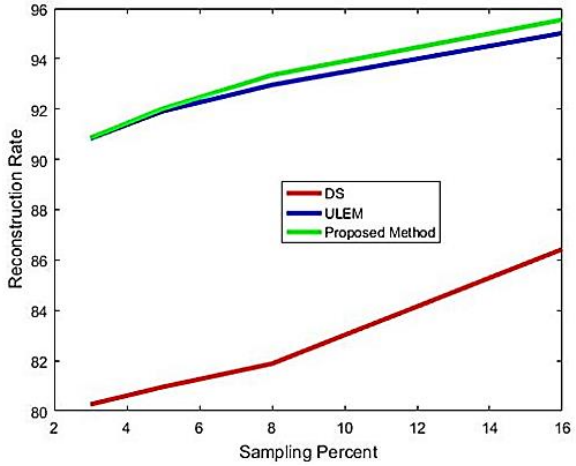

Figure 6. The reconstruction accuracy diagram of ULEM, DS and the proposed method in different sampling percentages on the Wall-Stone image.

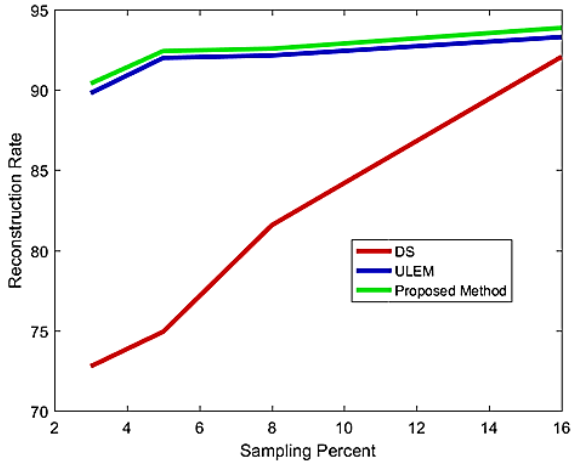

Figure 7. The reconstruction accuracy diagram of ULEM, DS and the proposed method in different sampling percentages on the Ti-Channel image.

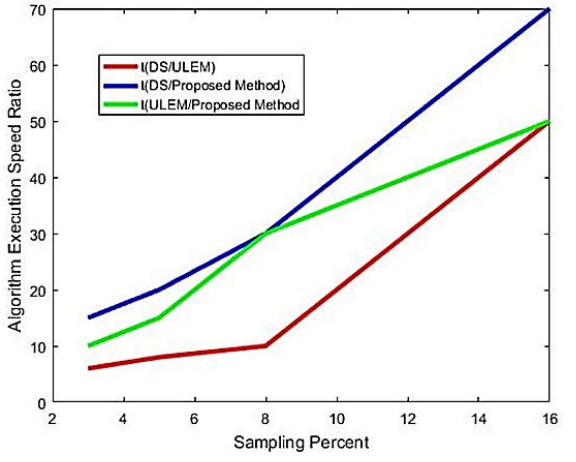

Figure 8. Comparison of algorithm execution time ratio.

one of 2^n states can be obtained. To solve this problem, the algorithms automatically increase the amplitude of the output state before measurement. These algorithms are known as amplitude amplification.

A slightly more complex quantum system is the one which contains two qubits of information, represented as:

$$\alpha|00\rangle + \beta|01\rangle + \Upsilon|10\rangle + \delta|11\rangle. \quad (4)$$

In this system, tow qubits can store four states simultaneously. This storage capacity rises exponentially with an increase in the number of qubits. For example, 50 qubits can hold $2^{50} \approx 10^{15}$ states. According to the principles of quantum computing, a quantum CPU can operate simultaneously on all these states. This property is called natural parallelism. In the classical regime, with a linear increase in the number of processors, the computing power can also increase linearly. However, in the quantum regime, with a linear increase in the number of qubits, the computing power increases exponentially.

Similar to classical digital circuits, there are unitary quantum gates represented in matrix form. These gates act on a qubit, and quantum algorithms consist of a set of these gates. Table 2 shows some of the most important single qubit gates along with the corresponding representation. The horizontal lines include a wire representing a qubit, and the symbols in the second column are a quantum gate acting on a qubit. For an input qubit $|\psi\rangle$, the output will be $U|\psi\rangle$. In Table 3, a number of conventional multi-qubit gates are shown along with the matrix representation. These gates affect several qubits. One of the most important quantum gates is the Hadamard gate, which is defined as follows:

$$H|j\rangle = 2^{\frac{-1}{2}}\left(|0\rangle + (-1)^j|1\rangle\right) \qquad with\ j = 0,1 \quad (5)$$

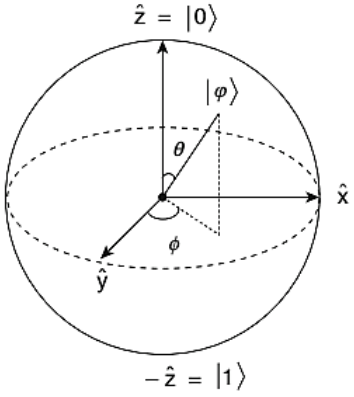

Figure 9. Baloch space.

Table 2. Single qubit gates.

Operator	Gate	Matrix
Pauli X	X	$\begin{bmatrix}0 & 1\\1 & 0\end{bmatrix}$
Pauli Y	Y	$\begin{bmatrix}0 & -i\\i & 0\end{bmatrix}$
Pauli Z	Z	$\begin{bmatrix}1 & 0\\0 & -1\end{bmatrix}$
Hadamard (H)	H	$\frac{1}{\sqrt{2}}\begin{bmatrix}1 & 1\\1 & -1\end{bmatrix}$
Phase (S,P)	S	$\begin{bmatrix}1 & 0\\0 & i\end{bmatrix}$
$\frac{\pi}{8}$ (T)	T	$\begin{bmatrix}1 & 0\\0 & e^{i\frac{\pi}{4}}\end{bmatrix}$

This gate plays an important role in quantum parallelism. One of the applications of this gate is to prepare the initial state. For example, if the initial state is $\underbrace{|00\ldots0\rangle}_{n}$, by applying n Hadamard gates, a superposition of states is created as follows:

$$|\psi_f\rangle = \alpha_0|00\ldots0\rangle + \alpha_1|00\ldots1\rangle + \cdots \alpha_{2^n}|11\ldots1\rangle. \quad (6)$$

Among the most important quantum gates is CNOT, which is a conditional gate. If the condition qubit is 1, the NOT gate is applied to

the input. Also, the Swap gate swaps the value of the high qubit with that of the low qubit. The Toffoli gate also works like CNOT, but instead of one control bit, it has two control bits and the NOT gate operates on the third input when two control bits are 1. As in classical computation, quantum registers are needed to increase efficiency. A set of qubits form a quantum register. The difference between classical and quantum registers is that while a classical n-bit register can only store a single value of 2^n possible states that occur with n bits, a n qubit register can store 2^n possible states created by n qubits. To compare classical and quantum processing power, imagine a classical 6-bit register that has $2^6 = 64$ different 6-bit words. A classical computer can process only one of these words at a time. To process 64 words simultaneously, we need 64 processors in parallel. This is easy nowadays. However, to simultaneously process all the states (80-bit register), 10^{24} processors are needed; which s not available today.

Table 3. Multi-qubit gates.

Operator	Gate	Matrix
Controlled Not (Cnot,Cx)	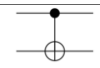	$\begin{bmatrix}1&0&0&0\\0&1&0&0\\0&0&0&1\\0&0&1&0\end{bmatrix}$
SAWP		$\begin{bmatrix}1&0&0&0\\0&0&1&0\\0&1&0&0\\0&0&0&1\end{bmatrix}$
Toffoli (CCNOT,CCX, TOFF)		$\begin{bmatrix}1&0&0&0&0&0&0&0\\0&1&0&0&0&0&0&0\\0&0&1&0&0&0&0&0\\0&0&0&1&0&0&0&0\\0&0&0&0&1&0&0&0\\0&0&0&0&0&1&0&0\\0&0&0&0&0&0&0&1\\0&0&0&0&0&0&1&0\end{bmatrix}$

At least in theory, it is possible to achieve a superposition of all 80 qubit states. Assume that the Hadamard gate is applied to all the qubits of the register. So, we will have:

$$H^{\otimes 80}\underbrace{|0\dots 00\rangle}_{80\ qubits} \equiv \frac{1}{\sqrt{2^{80}}}\left(\underbrace{|0\dots 00\rangle}_{80\ qubits}+\underbrace{|0\dots 10\rangle}_{80\ qubits}+\cdots\underbrace{|1\dots 11\rangle}_{80\ qubits}\right). \quad (7)$$

The above relationship has 10^{24} components. Based on quantum parallelism, any operation on this superposition state can be applied simultaneously to all states. In the classic regime, we will need 10^{24} processors to do this. Therefore, by increasing the number of qubits, we will achieve a very high processing power. In order to use quantum computation in image processing, it is first necessary to display the image in the form of quantum states. In the field of quantum image processing, the FRQI and NEQR methods are used to display a gray level image with size $2^n \times 2^n$ and gray range 2^q. The NEQR method requires q + 2n qubits to store the information of a gray level image [23]. The quantum image in NEQR is shown as follows:

$$|I\rangle = \frac{1}{2^n}\sum_{y=0}^{2^n-1}\sum_{x=0}^{2^n-1}|f(y,x)\rangle|yx\rangle = \frac{1}{2^n}\sum_{y=0}^{2^n-1}\sum_{x=0}^{2^n-1}\left|c_{yx}^{q-1}c_{yx}^{q-2}\dots c_{yx}^{0}\right\rangle|yx\rangle \quad (8)$$

In the above equation $\{c_{yx}^{q-1}, c_{yx}^{q-2}, c_{yx}^{q-3}\dots c_{yx}^{0}\} \in \{0,1\}$ and $f(y,x) \in \{0,1,\dots,2^q-1\}$. Compared to the other methods such as FRQI, this method causes quadratic speed-up in quantum image preparation and increases the compression ratio by about $1.5x$. As mentioned, to use the inherent properties of quantum parallelism, the initial states are usually written as a superposition of the states. Therefore, in quantum image processing, the input images must be written in superposition form using the NEQR method. Figure 10 shows an example of NEQR representation for a $2^2 \times 2^2$ image.

4. Comparison between quantum and classical methods

In this part, the quantum version of the median filter will be described and compared with classical methods in terms of computational complexity. In the classical median filter, a fixed window size 3×3 sweeps the entire image, and for each pixel of the noisy image, the median of the neighbors is placed in the center of the window. To perform the median filter at one point, the values of the pixels in the window are first sorted. Then, their median is determined and assigned to that pixel. Therefore, the logic of this filter is that the estimated pixels should be similar to their neighbors. To determine the median value of the pixels inside a window, the most common method is the Bubble sort [24]. However, this method has a high computational complexity. For this reason, in this article, as in reference [25], the following steps are performed on a window of the image. First, an ascending column sorting is performed. Row sorting, and finally right diagonal sorting will be carried out. These three steps used to determine the median of a window are called CRRD Sorting. An example of this median calculation method is shown in Figure 11. In the following, several basic modules, such as cycle-shift, swap, comparator, sort, and median calculation which are used in this article will be reviewed.

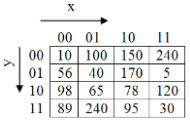

$$|I\rangle = \frac{1}{4}(|10\rangle\otimes|0000\rangle + |100\rangle\otimes|0001\rangle + |150\rangle\otimes|0010\rangle + |240\rangle\otimes|0011\rangle + |56\rangle\otimes|0100\rangle + |40\rangle\otimes|0101\rangle + |170\rangle\otimes|0110\rangle + |5\rangle\otimes|0111\rangle + |98\rangle\otimes|1000\rangle + |65\rangle\otimes|1001\rangle + |78\rangle\otimes|1010\rangle + |120\rangle\otimes|1011\rangle + |89\rangle\otimes|1100\rangle + |240\rangle\otimes|1101\rangle + |95\rangle\otimes|1110\rangle + |30\rangle\otimes|1111\rangle) = \frac{1}{4}(|00001010\rangle\otimes|0000\rangle + |01100100\rangle\otimes|0001\rangle + |10010110\rangle\otimes|0010\rangle + |11110000\rangle\otimes|0011\rangle + |00111000\rangle\otimes|0100\rangle + |00101000\rangle\otimes|0101\rangle + |10101010\rangle\otimes|0110\rangle + |00000101\rangle\otimes|0111\rangle + |01100010\rangle\otimes|1000\rangle + |01000001\rangle\otimes|1001\rangle + |01001110\rangle\otimes|1010\rangle + |01111000\rangle\otimes|1011\rangle + |01011001\rangle\otimes|1100\rangle + |11110000\rangle\otimes|1101\rangle + |01011111\rangle\otimes|1110\rangle + |00011110\rangle\otimes|1111\rangle)$$

Figure 10. An example of $2^2 \times 2^2$ image in the NEQR representation. (The symbol ⊗ indicates the tensor product between states).

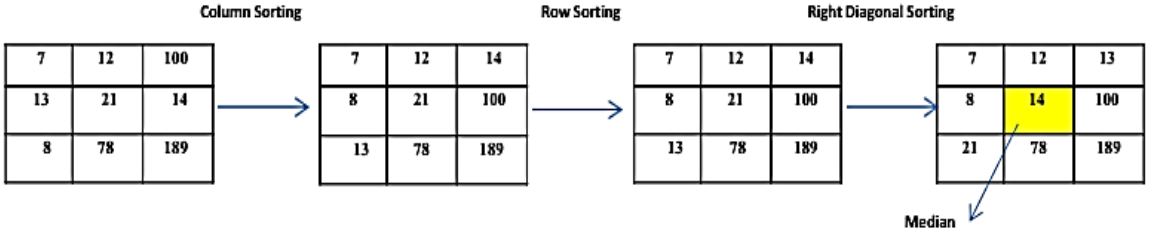

Figure 11. An example of the median calculation method (CRRD Sorting).

Cycle-shift modules: In this article, Cycle-shift modules, as provided in reference [26], are used to shift the points of a window. Four cycle shift modules are used in the construction of the quantum median filter. They are displayed as $s_{y-}, s_{y+}, s_{x-}, s_{x+}$ and their operation are as follows:

$$\begin{aligned} s_{y-}(|y\rangle) &= |(y-1) \mod 2^n\rangle \\ s_{y+}(|y\rangle) &= |(y+1) \mod 2^n\rangle \\ s_{x-}(|x\rangle) &= |(x-1) \mod 2^n\rangle \\ s_{x+}(|x\rangle) &= |(x+1) \mod 2^n\rangle \end{aligned} \quad (9)$$

The quantum circuits and an example of their operation are shown in figures 12 and 13. As shown, these gates cause the pixels to be translated by one unit. Therefore, according to the example presented in figure 13, by applying these modules to a window, the neighboring pixels can be obtained. We kindly refer readers to reference [26] for more information and details.

Swap module: As indicated in [27], we used this module to swap two gray level values. According to figure 14, if this module is applied, the values of two gray levels $|x\rangle$ and $|y\rangle$ will be swapped with each other.

Sort module: This module sorts three input integers in a descending order. It consists of three comparators and three Swap modules. Figure 15 shows an example of sort-out of three integers $|x\rangle$, $|y\rangle$ and $|z\rangle$ based on the presented method (figure 11) at the beginning of section 4. In this module, three comparisons must be made. First, $|x\rangle$ and $|y\rangle$ are compared with each other using the comparator module. If $e_1e_0 = 01$ (that is $|x\rangle > |y\rangle$), then $|x\rangle$ and $|y\rangle$ will be replaced by Swap module, otherwise there will be no change. After this step, similar to the previous steps, $|x\rangle$ is compared with $|z\rangle$, and $|y\rangle$ is compared with $|z\rangle$, and finally the sorted output will be $|x'\rangle$, $|y'\rangle$ and $|z'\rangle$.

Median module: According to figure 16 and the CRRD Sorting method, we will need seven sort modules to determine the median of a 3×3 window.

Quantum median filtering implementation and computational complexity analysis: The complete quantum median filtering circuit presented in this article is shown in figure 17. In the quantum median filter, eight separate images are first created using translation by one unit (up, down, left, right, up right, up left, down right and down left) from the original image. Similar to figure 13, this is done using cycle shift modules. This step is known as the Preparation Module. As for the nine images (eight images created in the previous step in addition to the main image), the median of the nine pixels in each (x, y) is calculated. This step is equivalent to sweeping the window over the entire image in the classical median filter.

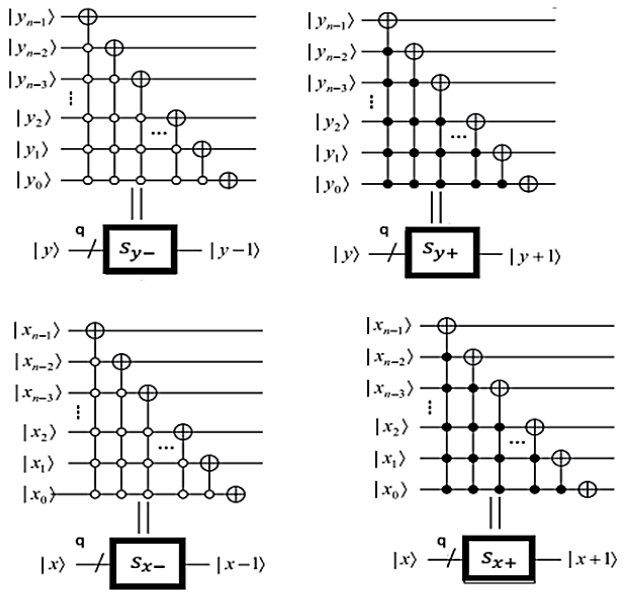

Figure 12. The cycle shift modules with the corresponding function and circuit.

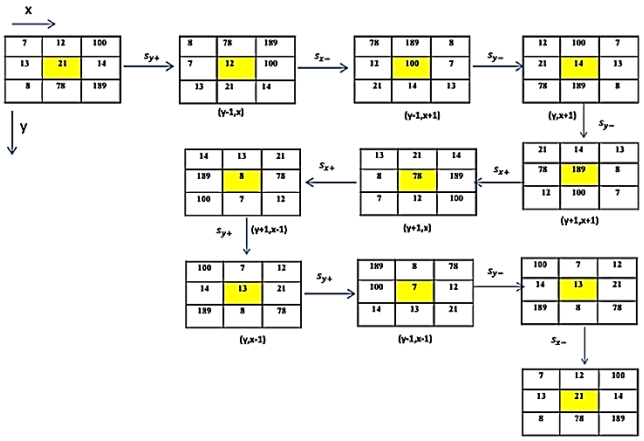

Figure 13. An example of the effects of the Cycle Shift module on an image window.

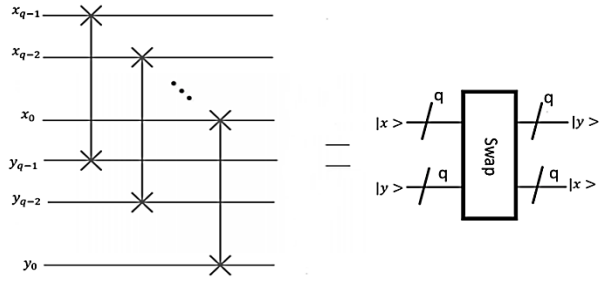

Figure 14. The swap module.

Since the NEQR model displays the image as a superposition of states, and due to the property of quantum parallelization, the median of all pixels is calculated simultaneously. To analyze the computational complexity of the quantum algorithm, the number of conventional gates used in each module should be first determined. Then, the different terms are added together to get the computational complexity of the whole algorithm. As shown in figure 17, the quantum median filter of this article consists of four different modules. According to reference [25], the image preparation module consists of ten cycle shifts and nine C-NOT; therefore, the complexity of this module will be $O(10n^2 + 9q)$.The median module also consists of seven sort modules as shown in figure 16. Also, according to figure 15, the sort module consists of three comparators and three swap modules. According to reference [28], the total complexity of this module is equal to $O(21q^2 + 63q)$. Also, based on the analysis done in reference [28], the complexity of Comparator module is equal to $O(q^2)$. As shown in figure 14, The swap module can be divided into three C-NOT gates. Thus, its complexity is $O(3q)$. Ultimately, the computational complexity of the entire quantum algorithm is equal to $O(10n^2 + 9q + 21q^2 + 63q + q^2 + 3q) = O(10n^2 + 22q^2 + 75q)$ which shows a comparable superiority over the classical version of the median filter. Since in the classical mode, the median value should be calculated for all points of the $2^n \times 2^n$ image, the computational complexity is the order of $O(2^{2^n})$. As a result, the computational complexity of the quantum median filter is improved by a polynomial order compared to its classical version., The idea of using the quantum median filter in image reconstruction, especially in high-dimensional images, has led to a significant reduction in the computational complexity. Therefore, in this part, a quantum median filter was implemented in reconstructing geological images. The steps of the proposed method are shown in figure 18. In the preprocessing stage, all the NAN points are first filled with salt and pepper noise. Then, using NEQR, the classical image is transformed into a quantum image (Classic to Quantum). In the next step, using cycle shift modules, 3×3 windows are extracted from the image. Then, using the median module, the median of the pixels in the window is calculated. In the next step, the central pixel is compared with the values of 0 and 255. If the central pixel is equal to either of these values (0 to 255), it will be replaced by the

median, otherwise the value of that pixel will not change. Finally, the reconstructed quantum image can be displayed in the form of a classical image using measurements (Quantum to Classic). Since we did not have access to a real quantum computer, all simulations were performed on a classical computer with a Corei7, 6GB RAM, and on MATLAB 2016 specifications. Also, for this reason, we did not report the execution time in this section. The reconstruction results of the proposed quantum median filter and DS method are shown in figure 19. It should be noted that, in this section, a simplified version of the quantum median filter was used for reconstructing geological images, and, the percentage of sampling is slightly higher than that of classical method presented in section 2. According to the results presented in figure 19, the reconstruction accuracy of the quantum median filter is acceptable compared to the DS in terms of quality. Also, according to the analysis done in this research, the complexity of the quantum median filter is $O(n^2)$, while the computational complexity of the DS is $O(2^{4n}m^2)$. It is worth mentioning that if the quantum median filter algorithm presented in this article is implemented on a real quantum computer, its execution speed will be exponentially faster than the DS method. The results obtained and the analysis done on computational complexity in this section show that quantum computing can be applied to other geological applications as well.

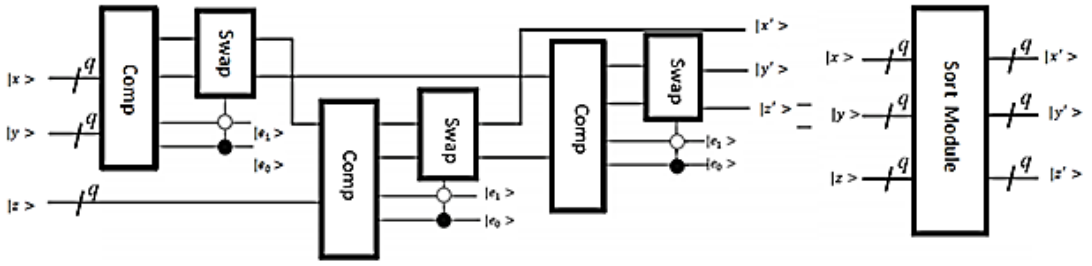

Figure 15. The sort module.

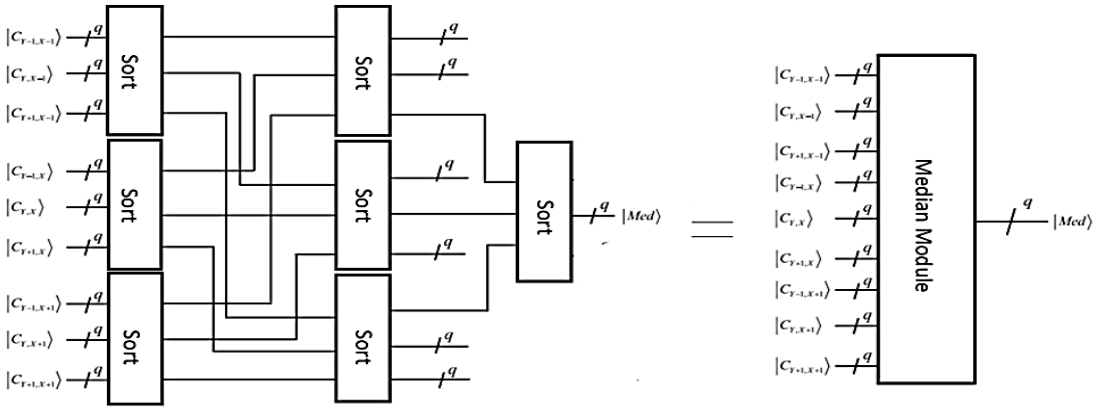

Figure 16. The median calculation module.

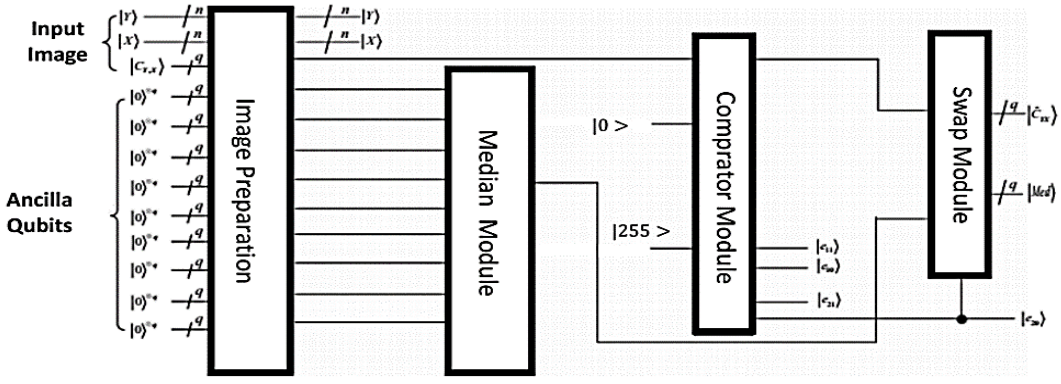

Figure 17. Complete quantum median filtering circuit.

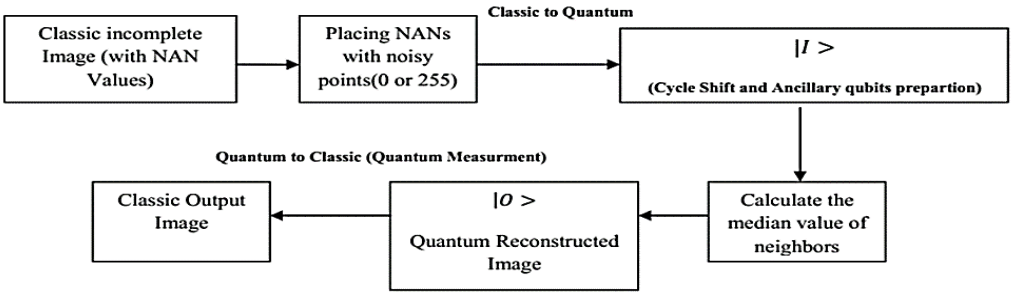

Figure 18. Schematic of quantum median filter.

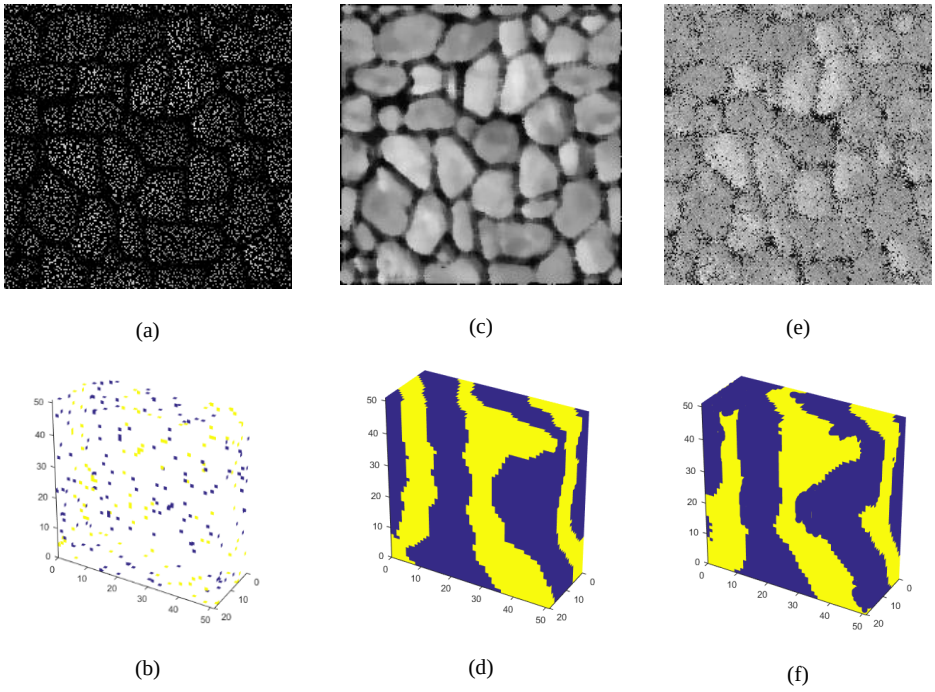

Figure 19. The Results of quantum median filter for the Wall-Stone and Delta binary image: (a) 20% sampling, (b) 8% sampling, (c) final image for Quantum Median Filter (Reconstruction Rate=92.50%), (d) final image for Quantum Median Filter (Reconstruction Rate=93.15%), (e) final Image for DS (Reconstruction Rate=80.53%),(f) final image for Ds (Reconstruction Rate=83.35%).

5. Conclusion

In this article, a geological image reconstruction method based on classical median and average filter was first presented. One of the advantages of this method is that it does not need training images. This method is much faster compared to the other methods, due to its use of median and means to estimate pixels. Also, selecting the window size adaptively in the proposed algorithm causes the estimated data to be similar to the original image. According to the results, it has high accuracy as well. The purpose of this study was to introduce the potential of quantum computing to the field of geosciences so that the researchers of this field can become more familiar with this computing method. When quantum computers become widespread, these researchers can benefit from their useful properties, one of which is the reduction of computing complexity. Therefore, in the second part of this article, quantum computing was briefly introduced and a quantum median filter was proposed for geological image reconstruction. The quantum median filter presented in this article was tested on two geological images, and its results were compared with the DS method. The results proved that the use of quantum computing in various geological problems can lead to higher efficiency of algorithms in terms of computational complexity.

Code availability section

Reconstruction-with-Spatial-Filter
Contact: sadeghkalantari@tafreshu.ac.ir
Software required: Matlab 2016
The source codes are available for downloading at the link: https://github.com/sadeghkalantari/Reconstruction-with-Spatial-Filter.git

REFERENCES

[1] Calderón, Hernán, Jorge F. Silva, Julián M. Ortiz, & Alvaro Egaña. (2015). Reconstruction of channelized geological facies based on RIPless compressed sensing. Computers & Geosciences, 77, 54-65. doi: https://doi.org/10.1016/j.cageo.2015.01.006

[2] Abdollahifard, Mohammad J., & Sadegh Ahmadi. (2016). Reconstruction of binary geological images using analytical edge and object models. Computers & Geosciences, 89 , 239-251. doi: https://doi.org/10.1016/j.cageo.2015.12.018

[3] Lee, Tai-Yong, & John H. Seinfeld. (1987). Estimation of two-phase petroleum reservoir properties by regularization. Journal

of Computational Physics, 69(2), 397-419. doi:https://doi.org/10.1016/0021-9991(87)90174-4

[4] Klise, Katherine A., Gary S. Weissmann, Sean A. McKenna, Elizabeth M. Nichols, Jedediah D. Frechette, Tim F. Wawrzyniec, & Vince C. Tidwell. (2009). Exploring solute transport and streamline connectivity using lidar based outcrop images and geostatistical representations of heterogeneity. Water Resources Research, 45(5). doi: https://doi.org/10.1029/2008WR007500

[5] Skøien, J. O., Merz, R., & Blöschl, G. (2006). Top-kriging-geostatistics on stream networks. Hydrology and Earth System Sciences, 10(2), 277-287. doi: https://doi.org/10.5194/hess-10-277-2006

[6] Emery, X. (2008). Uncertainty modeling and spatial prediction by multi-Gaussian kriging: accounting for an unknown mean value. Computers & geosciences, 34(11), 1431-1442. doi: https://doi.org/10.1016/j.cageo.2007.12.011

[7] Mahmud, K., G. Mariethoz, J. Caers, P. Tahmasebi, & A. Baker. (2014). Simulation of Earth textures by conditional image quilting. Water Resources Research, 50(4), 3088-3107.doi: https://doi.org/10.1002/2013WR015069

[8] Mariethoz, Gregoire, Philippe Renard, & Julien Straubhaar. (2010) .The Direct Sampling method to perform multiple point geostatistical simulations. Water Resources Research, 46 (11).doi: https://doi.org/10.1029/2008WR007621

[9] Kalantari, Sadegh, & Mohammad Javad Abdollahifard. (2016), Optimization-based multiple-point geostatistics: A sparse way."Computers & Geosciences,95, 85-98.doi: https://doi.org/10.1016/j.cageo.2016.07.006

[10] Abdollahifard, Mohammad J. (2016). Fast multiple-point simulation using a data-driven path and an efficient gradient-based search. Computers & Geosciences, 86, 64-74. doi: https://doi.org/10.1016/j.cageo.2015.10.010

[11] Pourfard, Mohammadreza, Mohammad J. Abdollahifard, Karim Faez, Sayed Ahmad Motamedi, & Tahmineh Hosseinian. (2017). PCTO-SIM: Multiple-point geostatistical modeling using parallel conditional texture optimization. Computers & Geosciences, 102, 116-138.doi: https://doi.org/10.1016/j.cageo.2016.12.012

[12] Strebelle, Sebastien. (2002). Conditional simulation of complex geological structures using multiple-point statistics. Mathematical Geology, 34(1), 1-21. doi:https://doi.org/10.1023/A:1014009426274

[13] Yang, Liang, Weisheng Hou, Chanjie Cui, & Jie Cui. (2016). GOSIM: A multi-scale iterative multiple-point statistics algorithm with global optimization. Computers & Geosciences, 89, 57-70. doi: https://doi.org/10.1016/j.cageo. 2015.12.020

[14] Sahimi, Muhammad, & Pejman Tahmasebi. (2022). The Potential of Quantum Computing for Geoscience. Transport in Porous Media, 1-21. doi: 10.1007/s11242-022-01855-8

[15] Nielsen, Michael A., & Isaac Chuang. (2002). Quantum computation and quantum information. doi: https://doi.org/10.1017/CBO9780511976667

[16] Harrow, A. W., Hassidim, A., & Lloyd, S. (2009). Quantum algorithm for linear systems of equations. Physical review letters, 103(15), 150502. doi:https://doi.org/10.1103/PhysRevLett.103.150502

[17] Lu, C. T., Chen, Y. Y., Wang, L. L., & Chang, C. F. (2016). Removal of salt-and-pepper noise in corrupted image using three-values-weighted approach with variable-size window. Pattern Recognition Letters, 80, 188-199. doi:https://doi.org/10.1016/j.patrec.2016.06.026

[18] Zhang, Peixuan, & Fang Li. (2014). A new adaptive weighted mean filter for removing salt-and-pepper noise. IEEE signal processing letters, 21(10), 1280-1283. doi: 10.1109/LSP.2014.2333012

[19] Kalantari, S., Ramezani, M., & Madadi, A. (2020). Introducing a New Hybrid Adaptive Local Optimal Low Rank Approximation Method for Denoising Images. International Journal of Industrial Electronics Control and Optimization, 3(2), 173-185. doi: https://doi.org/10.22111/ieco.2019.31245.1199

[20] Mariethoz, G., & Caers, J. (2014). Multiple-point geostatistics: stochastic modeling with training images. John Wiley & Sons.

[21] http://trainingimages.org

[22] Feynman, Richard P. (2018). Simulating physics with computers. Feynman and computation. CRC Press, 133-153.

[23] Wang, Zhaobin, Minzhe Xu, & Yaonan Zhang. (2021). Review of quantum image processing. Archives of Computational Methods in Engineering, 1-25. doi: https://doi.org/10.1007/s11831-021-09599-2

[24] Li, Panchi, Xiande Liu, & Hong Xiao. (2018). Quantum image median filtering in the spatial domain. Quantum Information Processing, 17(3), 1-25. doi: https://doi.org/10.1007/s11128-018-1826-9

[25] Jiang, S., Zhou, R. G., Hu, W., & Li, Y. (2019). Improved quantum image median filtering in the spatial domain. International Journal of Theoretical Physics, 58(7), 2115-2133. doi: https://doi.org/10.1007/s10773-019-04103-w

[26] Le, P. Q., Iliyasu, A. M., Dong, F., & Hirota, K. (2011). Strategies for designing geometric transformations on quantum images. Theoretical Computer Science, 412(15), 1406-1418. doi: https://doi.org/10.1016/j.tcs.2010.11.029

[27] Li, P., Liu, X., & Xiao, H. (2017). Quantum image weighted average filtering in spatial domain. International Journal of Theoretical Physics, 56(11), 3690-3716. doi: https://doi.org/10.1007/s10773-017-3533-1

[28] Wang, J., Jiang, N., & Wang, L. (2015). Quantum image translation. Quantum Information Processing, 14(5), 1589-1604. doi: https://doi.org/10.10 [2] Cargill, S.M., & Clark, A.L. (1978). Report on the activity of IGCP Project 98. J. Int. Assoc. Math. Geol., 10, 411-417. doi: https://doi.org/10.1007/BF02461973

[22] Nykänen, V., Groves, D.I., Ojala, V.J., Eilu, P., & Gardoll, S.J. (2008). Reconnaissance-scale conceptual fuzzy-logic prospectivity modeling for iron oxide copper-gold deposits in the northern Fennoscandian shield, Finland. Aust. J. Earth Sci., 55, 25–38. doi: https://doi.org/10.1080/08120090701581372

[23] Yousefi, M., & Carranza, E.J.M. (2016). Data-Driven Index Overlay and Boolean Logic Mineral Prospectivity Modeling in Greenfields Exploration. Nat. Resour. Res., 25, 3–18. doi: https://doi.org/10.1007/s11053-014-9261-9

[24] Yousefi, M., & Nykänen, V. (2017). Introduction to the special issue: GIS-based mineral potential targeting. J. African Earth Sci., 128, 1–4. doi: https://doi.org/10.1016/j.jafrearsci.2017.02.023

[25] Yousefi, M., & Nykänen, V. (2016). Data-driven logistic-based weighting of geochemical and geological evidence layers in mineral prospectivity mapping. J. Geochemical Explor., 164, 94–106. doi: https://doi.org/10.1016/j.gexplo.2015.10.008

[26] Dempster, A.P. (1968). A generalization of the Bayesian inference. J. R. Stat. Soc., 30, 205–447.

[27] Dempster, A.P. (1967). Upper and lower probabilities induced by a multivariate mapping.pdf. Ann. Math. Stat., 38, 325–339.

[28] Wang, J., Jiang, N., & Wang, L. (2015). Quantum image translation. Quantum Information Processing, 14(5), 1589-1604. doi: https://doi.org/10.1007/s11128-014-0843-6